# Computational study on sound scattering by jet shear layers

Laura Martin-Martin, Christophe Bogey, Vincent Clair, Gwenael Gabard

Aeroacoustics Conferences
June 4-7, 2024, Rome, Italy
30th AIAA/CEAS Aeroacoustics Conference (2024)

10.2514/6.2024-3183



# Computational study on sound scattering by jet shear layers

L. Martin-Martin[1,2*], C. Bogey[1†], V. Clair[1‡], and G. Gabard[3§]

[1] *Ecole Centrale de Lyon, CNRS, Université Claude Bernard Lyon 1, INSA Lyon, LMFA, UMR 5509, 69130, Ecully, France*
[2] *Siemens Digital Industries Software, Châtillon, 92320, France*
[3] *Laboratoire d'Acoustique de l'Université du Mans (LAUM), UMR 6613, Institut d'Acoustique - Graduate School (IA-GS), CNRS, Le Mans Université, Le Mans, 72000, France*

**The scattering and spectral broadening of sound waves by velocity and density fluctuations in the shear layers of jets with acoustic Mach numbers $M_a$ between 0.3 and 1.3 and temperatures between 1 and 2.25 times the ambient temperature are investigated numerically. For that, the propagation of acoustic waves generated by a monopolar source radiating at Helmholtz number $He$ = 2.7, 8.1 and 24.3 placed on the jet axis is simulated by solving the Linearized Euler Equations (LEE) using the Discontinuous Galerkin Method (DGM), with a base flow obtained from well-resolved Large Eddy Simulations. Two base flows consisting of the jet mean flow with or without axisymmetric flow fluctuations are considered. The objective is to analyze the effects of the flow fluctuations on the properties of the acoustic waves passing through the jet shear layers in space and in the frequency domain. The scattered field shows beams whose properties depend on the Mach number and the source frequency. The spatial scattering is evenly distributed throughout the domain, except upstream of the source for Mach numbers $M_j$ equal to 0.9, given the directivities of the acoustic fields. In the frequency domain, the spectra of the acoustic field show a tone and two lateral lobes. They are symmetric when the acoustic Mach number $M_a$ is at least 0.6 or at positions downstream of the source. For the heated jets, the lateral lobes in the spectra increase and approach the central peak as the temperature of the jets rises.**



## I. Introduction

During sound propagation in a turbulent medium, the acoustic waves properties change as they encounter disturbances. When the disturbances are time-independent, only the direction of propagation of the waves is modified, leading to spatial scattering. If the disturbances are convected, the waves are also affected by Doppler effect, which alters the frequency content of the sound. In particular, for an acoustic source radiating at a single frequency, the sound spectra may display a tone at the source frequency but also two lateral lobes. This phenomenon of energy redistribution in the frequency domain from the tone to the lateral lobes is named spectral broadening or haystacking.

Scattering and haystacking appear, for example, when conducting experiments in open wind tunnels, since the sound produced inside the flow has to pass through a turbulent shear layer before reaching the microphones placed in the far field. That makes the understanding of the mechanisms of sound generation difficult. To better understand these phenomena, Candel *et al.* [1–3] studied the acoustic field outside a wind tunnel for different Mach numbers and source positions. Experimental studies have also been conducted recently by Sijtsma *et al.* [4] and Kroeber *et al.* [5] for similar configurations. Numerical simulations providing turbulence and the acoustic field simultaneously are also possible using Direct Numerical Simulations (DNS) or Large Eddy Simulations (LES), as was done by Bennaceur *et al.* [6]. A less computationally expensive approach consists in generating a turbulent field with a stochastic method and then propagating acoustic waves through it by solving linearized equations. That was the case in the studies of Clair & Gabard [7] and Ewert *et al.* [8], who combined the Random Particule Mesh Method and a LEE solver to study spectral broadening by turbulent layers.

In the present study, the scattering and spectral broadening of sound waves by velocity, density and pressure fluctuations in the shear layers of jets with Mach numbers between 0.3 and 1.3 and temperatures between 1 and 2.25

*PhD student, laura.martin@ec-lyon.fr
†CNRS Research Scientist, christophe.bogey@ec-lyon.fr. AIAA Senior Member and Associate Fellow.
‡Assistant professor, vincent.clair@ec-lyon.fr
§Professor, gwenael.gabard@univ-lemans.fr. Senior Member AIAA.

times the ambient temperature are investigated numerically. The sound propagation is simulated using a solver of the 2-dimensional Linearized Euler Equations based on the Discontinuous Galerkin Method (DGM). In practice, a source is placed on the jet axis and radiates waves propagating over a base flow obtained previously. The time-dependent base flow is obtained from a $(x, r)$ section of 3-dimensional round jets computed by recent LES [9–11]. The base flows turbulence considers only the first azimuthal mode $n_\theta = 0$. The effects of the jet Mach number, temperature and source frequency on the acoustic waves traveling across the unsteady shear layer are investigated.

This article aims to study the effects of the shear-layer turbulence on the spatial scattering and the haystacking for jets at high Mach numbers. The last objective is to discuss the links between the properties of the turbulence fluctuations and spectral content of the acoustic field.

This article is structured as follows. Section II presents the main parameters of the LES simulations and documents the base flow properties. The numerical parameters of the DGM simulations are presented in Sec. III. The spatial scattering of the acoustic waves is studied in Sec. IV and the spectral broadening of the sound is discussed in Sec. V. Concluding results are provided in Sec. VI.



## II. LES jet flow

### A. Jets parameters

The turbulent shear layers considered in this study have been obtained in recent Large Eddy Simulations (LES) of round free jets performed*[9, 10, 12–16]. The LES code is implemented with low-dissipation and low-dispersion finite-difference schemes. A fourth-order 11-point centered finite-difference method is applied for the spatial discretization, while the time integration is carried out using a second-order six-stage low-storage Runge–Kutta scheme. The LES solves the compressible Navier–Stokes equations written in cylindrical coordinates $(r, \theta, x)$, on a domain extending over $0 \leq r/r_0 \leq 15$, $0 \leq \theta < 2\pi$ and $0 \leq x/r_0 \leq 40$, where $r_0 = D/2$ is the radius of the jet and the jet nozzle-exit is at $x = 0$. Since the DGM simulations are performed in 2 dimensions, only the LES data in slices at $\theta = 0$ and $\theta = \pi$ for the axisymmetric are used in this work.

The main parameters of the jets are provided in Table 1. They include the acoustic Mach number of the jet relative to the ambient speed of sound $M_a = u_j/c_a$, the jet Mach number relative to the speed of sound in the jet $M_j = u_j/c_j$, the ratio between the temperature in the jet and the ambient temperature $T_j/T_a$ and the diameter-based Reynolds number $Re_D = u_j D/\nu_j$. The velocity $u'_e$ is the peak root-mean-square value of the axial velocity fluctuations at the nozzle-exit, $u_j$ is the jet velocity at the nozzle exit and $\nu_j$ the kinematic molecular viscosity in the jet. In this study, three isothermal jets with Mach numbers of 0.3, 0.6 and 0.9, referred to as IsoM03, IsoM06 and IsoM09 are considered. Two heated jets at $M_a = 0.9$ with temperature ratios $T_j/T_a = 1.5$ and 2.25, denoted as T1Ma09 and T2Ma09, respectively, and two jets at $M_j = 0.9$ with $T_j/T_a = 1.5$ and 2.25, namely T1Mj09 and T2Mj09 are also considered. In all cases, the Reynolds number is similar to $10^5$ and the nozzle-exit peak turbulence intensity is equal to 9%. During the LES, the flow variables have been recorded over times typically of $10^3 r_0/u_j$. In particular, the flow fluctuations, decomposed into the first 9 azimuthal modes $n_\theta = 0, \ldots, 8$, have been stored in the $(x, r)$ planes. Only the first azimuthal mode $n_\theta = 0$ is used for the 2-dimensional DGM simulations.

| | $M_a$ | $M_j$ | $T_j/T_a$ | $Re_D$ | $u'_e/u_j$ | time simulations | references |
|---|---|---|---|---|---|---|---|
| IsoM03 | 0.3 | 0.3 | 1.0 | $1e5$ | 9% | 694 $r_0/u_j$ | [12–14] |
| IsoM06 | 0.6 | 0.6 | 1.0 | $1e5$ | 9% | 1111 $r_0/u_j$ | [12–14] |
| IsoM09 | 0.9 | 0.9 | 1.0 | $1e5$ | 9% | 1375 $r_0/u_j$ | [12–14] |
| T1Ma09 | 0.9 | $\simeq 0.73$ | 1.5 | $2e5$ | 9% | 1250 $r_0/u_j$ | [10, 15] |
| T2Ma09 | 0.9 | $\simeq 0.6$ | 2.25 | $4e5$ | 9% | 1125 $r_0/u_j$ | [10, 15] |
| T1Mj09 | 1.1 | $\simeq 0.9$ | 1.5 | $2e5$ | 9% | 1345 $r_0/u_j$ | [16] |
| T2Mj09 | 1.3 | $\simeq 0.9$ | 2.25 | $4e5$ | 9% | 1271 $r_0/u_j$ | [16] |

**Table 1 Parameters of the jets.**

*The LES data are accessible upon request by email to christophe.bogey@ec-lyon.fr. Further information can be found in https://acoustique.ec-lyon.fr/JetNoiseData/LESdatabase_freejets.pdf.

### B. Base flow properties

The jet shear-layer thickness is estimated from the jet mean flow by calculating the momentum thickness

$$\delta_\theta(x) = \int_0^{r_{2\%}(x)} \frac{\bar{u}(x,r)}{u_j}\left(1-\frac{\bar{u}(x,r)}{u_j}\right) dr, \tag{1}$$

where $\bar{u}$ is the time-averaged axial velocity and $r_{2\%}(x)$ is the value of $r$ such that $\bar{u}(x,r) = 0.02u_j$. The axial variations of the momentum thickness obtained for the different jets are shown in Fig. 1. The thickness increase almost linearly in all cases, as expected [10]. In Fig. 1a, the momentum thicknesses of the isothermal jets are compared. The curves are superposed for $x/r_0 \leq 2$. For $x/r_0 > 2$, the thicknesses grow at different rates. The lowest rate is obtained for IsoM09, which means that at a given axial position, the shear layer is thinner as the Mach number increases. The momentum thickness for jets at $M_a = 0.9$ and $M_j = 0.9$ at different temperatures are shown in Fig. 1b. Considering IsoM09 as the case of reference, varying the temperature $T_j$ between $T_a$ and $2.25T_a$ at $M_a = 0.9$ makes the shear layer spread more rapidly. In contrast, the momentum thicknesses obtained at $M_j = 0.9$ are very similar regardless the jet temperature.

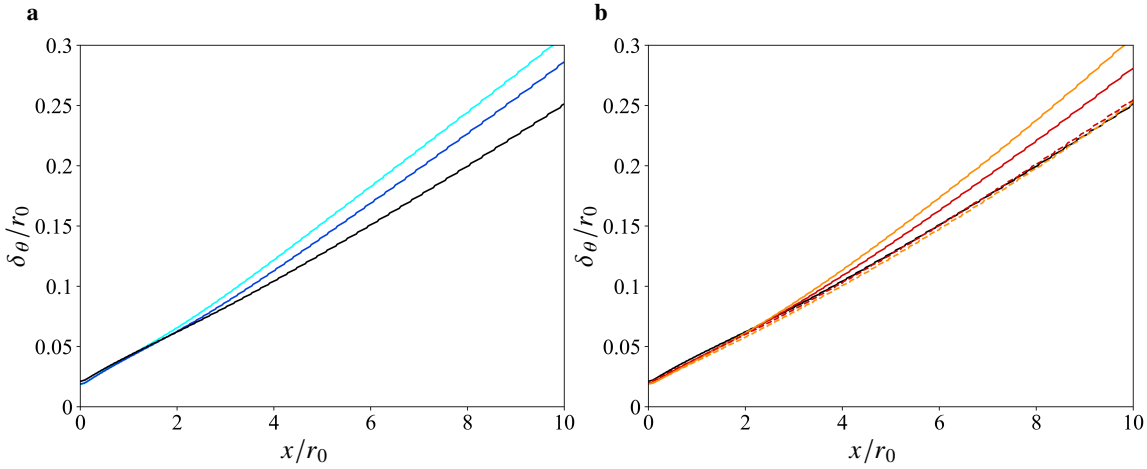


**Fig. 1 Axial variations of the shear-layer momentum thickness $\delta_\theta/r_0$ for (a) isothermal jets and (b) jets at $M_a = 0.9$ and $M_j = 0.9$. IsoM03, IsoM06, IsoM09, T1Ma09, T2Ma09, T1Mj09 and T2Mj09.**

The properties of the jet flows are characterized. The temperature fluctuations are represented by the density fluctuations. The spectra of the radial velocity and density fluctuations obtained inside the shear layer at $x/r_0 = 4$, $r/r_0 = 1$, in the vertical of the source position, for the azimuthal mode $n_\theta = 0$ are shown in Fig. 2 as a function of the Strouhal number $St_D = fD/u_j$. They all show a hump located around $St_D \simeq 0.5$. In Camussi & Bogey [17], similar spectra were obtained for the pressure fluctuations of the jet IsoM09 at $x/r_0 = 4$, $r/r_0 = 2$.

The levels calculated for the radial velocity fluctuations in Fig. 2a are lowest for the jet IsoM09, and they increase with the temperature or when the Mach number decreases. The highest levels, obtained for T2Ma09, are one order of magnitude higher than those for IsoM09. In the spectra of the density fluctuations shown in Fig. 2b, the levels increase between IsoM030 and IsoM060, but do not change much between IsoM06 and IsoM09. The increase is more pronounced when the ratio $T_j/T_a$ rises. The peak values for heated the jets at $M_j = 0.9$ T1Mj09 and T2Mj09 are similar to those for T1Ma09. The difference between the levels obtained between IsoM09 and T2Ma09 is of almost two orders of magnitude. Thus, the amplitudes of the density fluctuations vary more from one jet to another than the amplitudes of the velocity fluctuations. This is expected given that for hot jets, the magnitude of the density fluctuations should scale as the difference in density $|\rho_j - \rho_a|$ [18].

The peak Strouhal numbers in the radial velocity and density spectra, obtained along $r/r_0 = 1$, are plotted in Fig. 3 as a function of $x/r_0$. The variations of the peak $St_D$ in the density spectra in Fig. 3b are very similar to those for the radial velocity. In all the cases, the curves decrease in the downstream direction. The decrease is faster near the nozzle exit than farther downstream. In Fig. 3a for the radial velocity, similar results are obtained for the isothermal jets IsoM03, IsoM06, IsoM090 and the heated jet T2Mj09, with peak $St_D$ varying from $St_D = 1.5$ down to $St_D = 0.5$ between $x/r_0 = 1$ and $x/r_0 = 8$. Lower $St_D$ values are obtained for the other hot jets. The lowest values are found for T2Ma09 and T1Mj09. The levels for these two jets decrease from $St_D = 1$ down to $St_D = 0.35$ between $x/r_0 = 1$ and $x/r_0 = 8$.

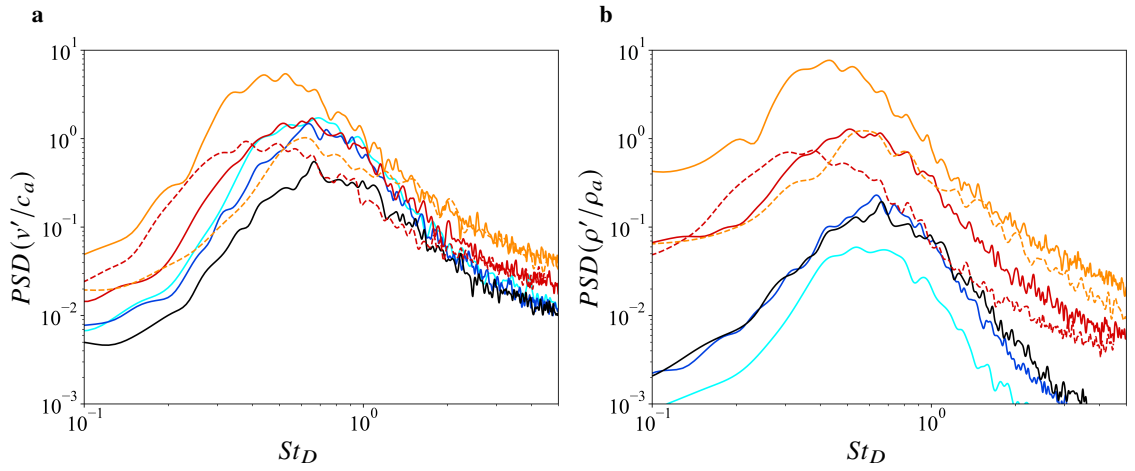


**Fig. 2 Power Spectral Densities of (a) the radial velocity fluctuations $v'/c_a$ and (b) the density fluctuations $\rho'/\rho_a$ at $x/r_0 = 4$, $r/r_0 = 1$ for the azimuthal mode 0 for — IsoM03, — IsoM06, — IsoM09, — T1Ma09, — T2Ma09, - - - T1Mj09, - - - T2Mj09.**

To explain the variation of the $St_D$ peak values, it can be noted that the peak Strouhal number is most likely proportional to the passing frequency of the most energetic structures. According to Fig. 1, the increase of the shear-layer thickness, and therefore of the size of the turbulent structures, can be approximated by a linear function $w(x) = ax$. Since the velocity of the mean base flow is almost constant and close to $0.6u_j$ along $r/r_0 = 1$ upstream of the end of the potential core, the passing frequency of these structures varies approximately as $1/w(x) \propto 1/x$. A curve representing this function is plotted in Fig. 3. It agrees qualitatively well with the curves obtained for the $St_D$ peak values.

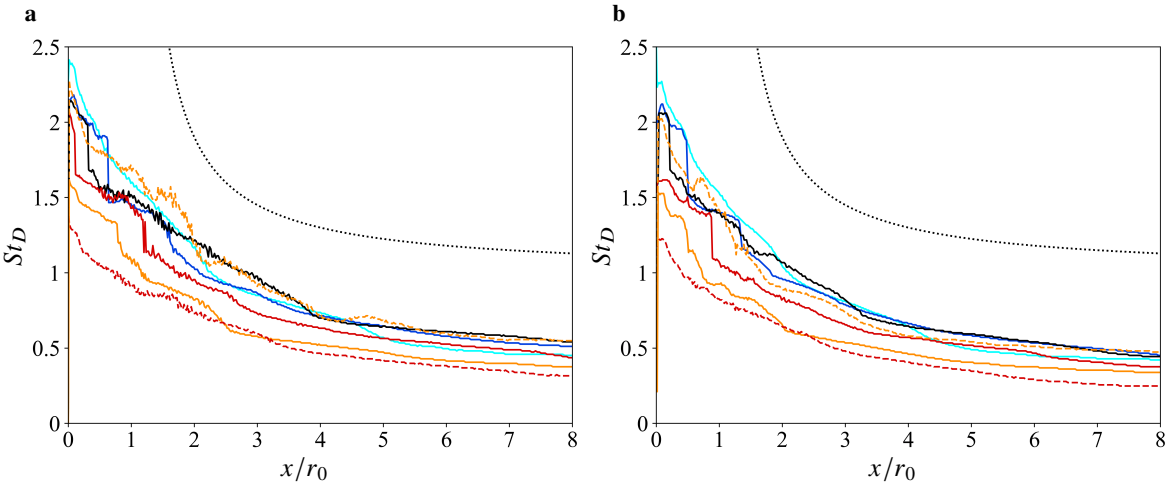


**Fig. 3 Axial variations of the peak Strouhal number in the PSD obtained along $y = r_0$ for (a) the radial velocity fluctuations and (b) the density fluctuations for — IsoM03, — IsoM06, — IsoM09, — T1Ma09, — T2Ma09, - - - T1Mj09, - - - T2Mj09, ··· function proportional to $1/x$.**

## III. Parameters of the acoustic simulations

The propagation of the acoustic wave generated by a source placed on the jet axis at $x/r_0 = 4$ radiating at different frequencies is computed using a DGM code developed at Siemens [19]. The code solves the Linearized Euler Equations in a conservative form with the pressure variable $p'$ substituted by the Goldstein pressure $\pi'$ [20]. The time integration is performed by a 6-stage, optimized, low-storage Runge-Kutta scheme [21]. A computational domain of size $0 \leq x \leq 60r_0$

and $-5.5r_0 \leq y \leq 5.5r_0$ is used, where $r_0$ is the jet radius. Two mesh grids are used in this study: both are discretized by an unstructured mesh made of triangular elements, and divided into two parts, namely a physical domain for $r_0 \leq x \leq 8r_0$ and $-4.5r_0 \leq y \leq 4.5r_0$, and a buffer zone everywhere else. The size of the elements is not uniform throughout the physical domain. When the source radaites at Helmholtz number $H_e = fD/c_a \leq 8.1$, the elements side length is equal to $h = r_0/20$ at the borders of the physical domain. It decreases as the elements are closer to the region $r_0 \leq x \leq 4r_0$, $-r_0 \leq y \leq r_0$, in which $h = r_0/71$. This ensures at least 7 nodes per wavelength for the waves propagating upstream inside the jet in all cases. When the source radiates at Helmholtz numbers in the range $8.1 < H_e \leq 24.3$, the elements are three times smaller to also ensure at least 7 nodes per wavelength. Inside each element, the solution is computed with a polynomial of degree $N = 4$, providing a mean distance between nodes $\Delta$ equal to $h/4$. The elements in the buffer zone are stretched downstream $x = 8r_0$ at a rate of 2.5%. To improve the damping in the buffer zone, the filter proposed by Hesthaven and Warburton [22] is implemented. The non-reflecting characteristic boundary conditions are applied at the outer boundary. A high-order filter with cut-off order $N_c = N - 1$ is applied throughout the computational domain to remove high-frequency oscillations. The $CFL$ condition is defined as

$$CFL = \Delta t \max\left\{\frac{u^e_{max}}{\Delta_{min} r^e}\right\},$$

where $u^e_{max}$ is the maximal phase speed inside the element $e$, $\Delta_{min}$ is the minimal distance between nodes in an equilateral triangle of reference of size $h = 1$, and $r^e$ is the radius of the inscribed circle, i.e. the maximal circumference contained in the element $e$. The CFL number is fixed at 2 ensuring stability in all cases.

To introduce the LES flow fields in the base flow of the DGM simulations, the LES data are interpolated at every DGM node and at every simulation time step. The interpolations are carried out using a polynomial of degree 5 in time and of degree 1 in space.

The acoustic source in the DGM simulations is a Gaussian monopole placed on the jet axis at $x/r_0 = 4$. It is introduced on the right-hand side of the Linearized Euler Equations as the following source term

$$\begin{cases} s_{\rho'}(x,y) & = A\sin(\omega_0 t)\exp\left(-\ln(2)\dfrac{(x-x_c)^2-(y-y_c)^2}{b^2}\right), \\ s_{(\rho u)'}(x,y) & = \rho'(x,y)u_0(x,y), \\ s_{(\rho v)'}(x,y) & = \rho'(x,y)v_0(x,y), \\ s_{\pi'}(x,y) & = \dfrac{\pi_0(x,y)}{\rho_0(x,y)}\rho'(x,y). \end{cases} \tag{2}$$

where $\omega_0$ is the angular frequency, $b$ is the half-width of the Gaussian source equal to $\Delta$, $x_c = 4r_0$, $y_c = 0$ and $A$ is the source amplitude.

The simulations are performed for different source frequencies corresponding to Helmholtz numbers $H_e = 2.7$, 8.1 and 24.3. The wavelengths obtained when the acoustic waves propagate at speeds $c_a$, $c_a(1 - M_a)$ and $c_a(1 + M_a)$ are shown as a function of the jet acoustic Mach number in Fig. 4a, Fig. 4b and Fig. 4c, respectively. When the waves propagate in the surrounding medium at rest or inside the jet in the downstream direction, the wavelengths do not greatly change with the Mach number. In contrast, the wavelengths shortens significantly for waves propagating upstream of the source inside the jet when $M_a$ increases, especially around $M_j = 0.9$. In particular for IsoM09, the wavelength is almost 20 times shorter for the waves propagating upstream than downstream inside the jet. The data obtained from the DGM simulations inside the physical domain are saved at points equally spaced every $r_0/37.5$, four times per period of the acoustic source. In particular, those points located at a distance of $3r_0$ from the source at angles $\psi = 45°$, 90° and 135° are noted as $M_{45°}$, $M_{90°}$ and $M_{135°}$.

To avoid the growth of numerical oscillations in the buffer zones, the LES fluctuations are attenuated progressively outside the physical domain. That is achieved by smoothly damping the amplitude of the LES base flow fluctuations.

## IV. Spatial scattering

### A. Pressure fields

The pressure fields obtained for a source radiating at $H_e = 8.1$ for IsoM03, IsoM09 and T2Ma09 are shown in Fig. 5. The pictures on the left display the pressure fields $p'_{meanflow}$ obtained with the LES mean flow. Outside the jet, the wavefronts are elongated in the downstream direction, especially as the Mach number increases. Inside the jet,

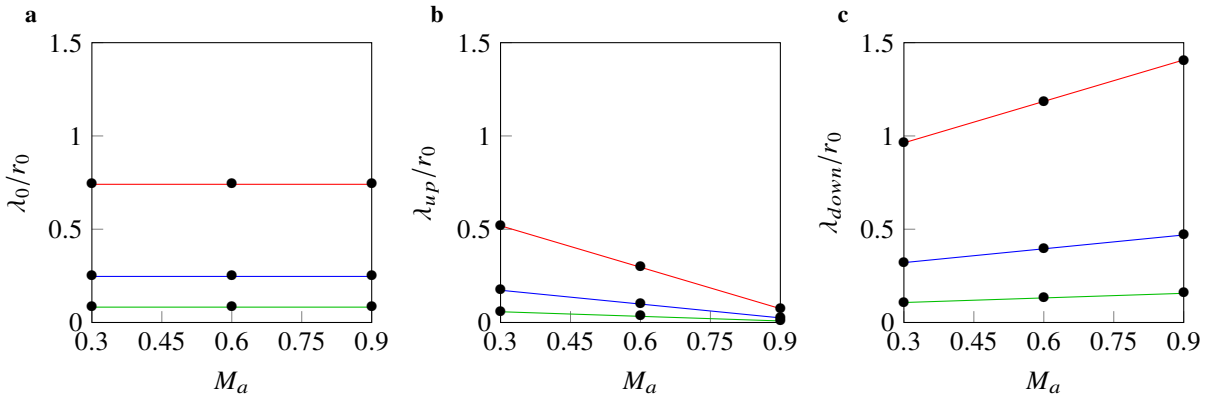


**Fig. 4 Variation of the ratios (a) $\lambda_0 = c_a/f_0$, (b) $\lambda_{up} = c_a(1 - M_a)/f_0$ and (c) $\lambda_{down} = c_a(1 + M_a)/f_0$ as a function of $M_a$ when the acoustic waves propagate in the medium at rest, inside the jet in the upstream and downstream directions, respectively; — $H_e = 24.3$, — $H_e = 8.1$ and — $H_e = 2.7$.**

the wavelengths of the waves propagating upstream decrease and their amplitudes increase for a higher Mach number. For the two jets at $M_a = 0.9$, the wavelengths are larger and the pressure levels are lower inside the jet upstream and downstream for T2Ma09 than for IsoM09. This is due to the increase in the jet temperature, which leads to a sound speed $c_j$ inside the flow of $1.5c_a$ for T2Ma09.

The pressure fields $p'_{n_\theta=0}$ obtained using the LES unsteady base flow for $n_\theta = 0$ are shown in the middle pictures of Fig. 5. The general trends are the same as those obtained using the LES mean flow only. The effects of the flow fluctuations are visible outside the flow, where large elongated regions with maximum pressure levels different from those obtained without fluctuations are observed. These regions will be referred to as beams hereafter. For the case IsoM09 in Fig. 5(e), small regions with high-frequency oscillations of much higher pressure levels than those obtained with the mean flow are also observed for $x/r_0 \leq 3$. They will be denoted as high-frequency spots.

The differences between the pressure fields $p'_{n_\theta=0}$ and $p'_{meanflow}$, namely the scattered pressure fields $p'_{scat}$, are shown in the right pictures of Fig. 5. The radial velocity fluctuations in the flows are represented with black isocontours for $v'/u_j = \pm 0.015, \pm 0.03, \pm 0.05$ and $\pm 0.07$. Rounded zones in which the radial velocity is alternatively positive and negative are observed along the shear layer. They correspond to the largest turbulent structures. The beams here are delimited by lines along which the pressure level $p'_{scat}$ is zero due to destructive interferences. The beams seem to be related to the turbulent structures in the shear layers. In particular, the beams seems to be attached to the center of the zones with strong radial velocity, while the lines of destructive interferences pass in between, where the radial velocity is zero. This is due to the fact that the radial velocity fluctuations are zero, and then the acoustic waves are not affected by the fluctuations. The beams are more curved as the convection velocity of the turbulent structures increases, as found in [23] for convected isolated vortices. The amplitudes of the beams are similar to the levels of the pressure fields $p'_{meanflow}$ for IsoM09 and T2Ma09, but lower for IsoM03. In addition, the amplitude of the scattered fields inside the jet is around 200 times than $p'_{meanflow}$ outside the flow for IsoM090. The levels of $p'_{scat}$ for IsoM03 and T2Ma09 are lower, but they are not zero. This implies that the fields obtained with the mean flow and the flow fluctuations differ in the jet core, specially for IsoM09. The high-frequency spots observed for IsoM09 in Fig. 5(f) upstream of the source are not organized as the beams. Therefore, they may be caused by a different phenomenon.

The scattered pressure fields $p'_{scat}$ obtained for $H_e = 2.7$, 8.1 and 24.3 for the jet IsoM030 are shown in Fig. 6. The large beams mentioned previously, can be seen in the three cases. They have approximately the same curvature in the three cases. The ratio between the maximal pressure levels of the scattered fields and the peak level obtained with the mean flow at $M_{90°}$ is 0.19 for $H_e = 2.7$ in Fig. 6a. This ratio increases with the Helmholtz number up to 1.41 for $H_e = 24.3$ in Fig. 6c. This is because, given that the base flow properties are the same in the three cases, the acoustic waves in $p'_{n_\theta=0}$ are displaced the same distance with regard to their positions in $p'_{meanflow}$ for all the source frequencies. When the wavelength is shorter, this leads to a greater phase shift of the waves resulting in more important pressure levels differences between $p'_{n_\theta=0}$ and $p'_{meanflow}$. The central beam is wider in Fig. 6b than in Figs. 6a and 6c. The zones of radial velocity associated with these beams are also larger in Fig. 6b, extending over $4 \lesssim x/r_0 \lesssim 6$, than in Figs. 6a and 6c, lying only between $4 \lesssim x/r_0 \lesssim 5$. This confirms the connection between the beams in the scattered field and the largest turbulent structures.

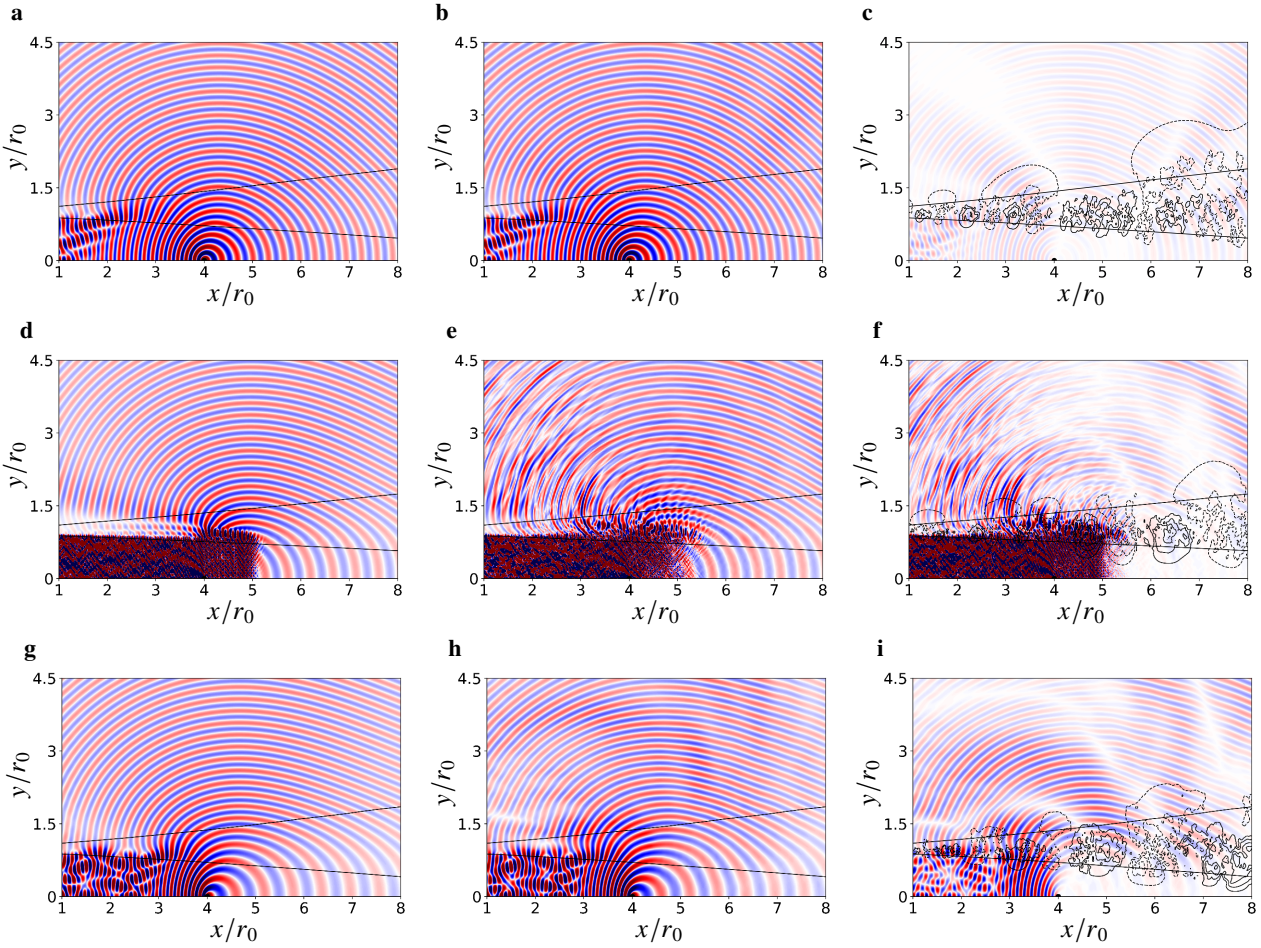


**Fig. 5 Pressure fields obtained with the (left) mean flow, (middle) unsteady flow with $n_\theta = 0$ and (right) scattered fields for the jets (a-c) IsoM03, (d-f) IsoM09 and (g-i) T2Ma09. The source radiates at $H_e = 8.1$; The colormap colors vary between −4 and 4 times the maximal $p'_{mean\,flow}$ value at $M_{90^\circ}$; (——) $\bar{u}/u_j = 0.05$ and 0.95; (——) Positive and (– – –) negative isocontours $v'/u_j = \pm 0.015, \pm 0.03, \pm 0.05$ and $\pm 0.07$.**

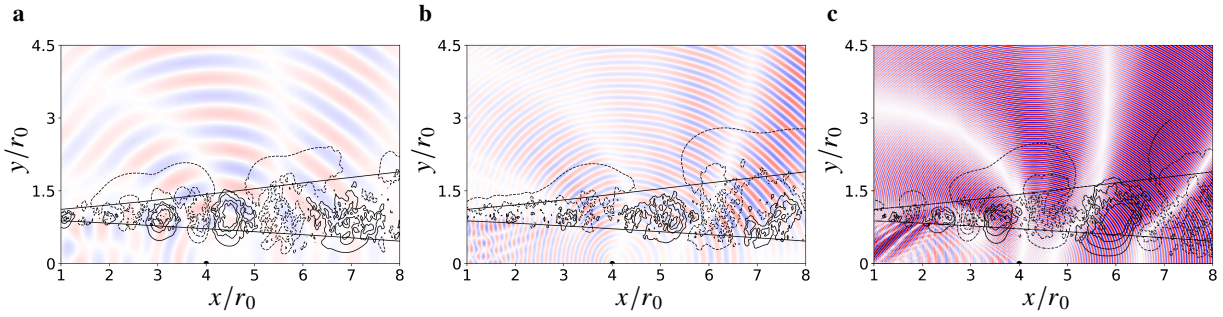


**Fig. 6 Scattered pressure fields for the jet IsoM03 at (a) $H_e = 2.7$, (b) $H_e = 8.1$ and (c) $H_e = 24.3$. The colormap colors vary between −2 and 2 times the maximal $p'_{mean\,flow}$ value at $(x/r_0 = 4, y/r_0 = 3)$; (——) $\bar{u}/u_j = 0.05$ and 0.95; (——) Positive and (– – –) negative isocontours $v'/u_j = \pm 0.015, \pm 0.03, \pm 0.05$ and $\pm 0.07$.**

### B. Directivity fields

The rms pressure levels obtained at $3r_0$ from the source using the mean flow for the three isothermal jets for $H_e = 8.1$ are shown in Fig. 7a as a function of $\psi$. They are normalized by the levels at $M_{90^\circ}$. The results for $H_e = 2.7$ and

24.3 are similar than those for $H_e = 8.1$. For the jet IsoM03, the normalized levels vary by less than 0.13 between $\psi = 60°$ and 140°, reaching their maximum value at $\psi \simeq 70°$. For IsoM06, they are also maximum at $\psi = 70°$, but they decrease faster as $\psi$ tends to 160° than for IsoM030. For IsoM09, the levels show a hump centred around $\psi = 65°$, and a maximum value 0.1 higher than for the other two cases. The oscillations observed near $\psi = 160°$ are due to constructive and destructive interferences visible in Fig. 5(d), in the shear-layer region.

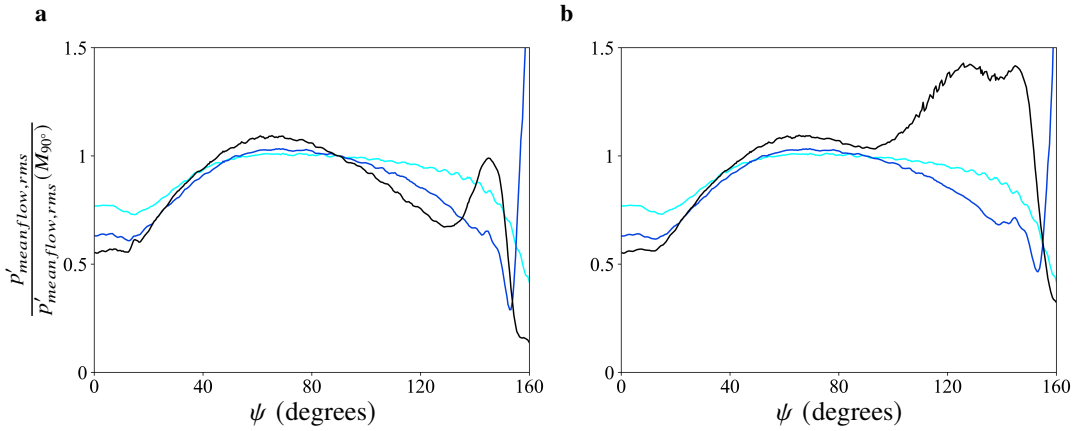


**Fig. 7 Normalized rms pressure levels obtained at $3r_0$ from the source using (a) the mean flow and (b) the flow fluctuations $n_\theta = 0$ for — IsoM03, — IsoM06 and — IsoM09. The source radiates at $H_e = 8.1$.**

The rms pressure levels obtained using the unsteady base flow normalized by the level obtained with the mean flow at $M_{90°}$, are shown for the three isothermal jets in Fig. 7b. Compared with Fig. 7a, the directivity is similar for IsoM03 and IsoM06, but significantly differs for IsoM09, for which a bump reaching values close to 1.4 clearly emerges for $\psi > 100°$. The position of the bump coincides with the region at $x/r_0 \leq 3$ where the high-frequency spots are visible in Fig. 5(e).

The rms pressure levels obtained with the mean base flows and the unsteady base flows for $n_\theta = 0$ normalized by the level obtained with the mean flow at $M_{90°}$ are plotted for all the jets at $M_a = 0.9$ and $M_j = 0.9$ in Fig. 8. For the mean base flows, the peak level angle is shifted from $\psi = 65°$ to 80° when the temperature of the jet $T_j$ rises up to $T_a = 2.25$ for the jets at $M_a = 0.9$. At the same time, the peak level is reduced by 0.1 and the levels at $\psi > 90°$ increase. The changes in level for the jets at $M_j = 0.9$ are less marked. The peak level angle moves from $\psi = 65°$ to 75° and the peak value decreases only by 0.05 between $T_j = T_a$ and $T_j = 2.25T_a$. The levels obtained for the hot jets with $M_a = 0.9$ are similar to those obtained with the mean flow. Different trends are found for the jets at $M_j = 0.9$. In particular, a hump appears at $\psi > 120°$ for T1Mj09 and T2Mj09. The height of the hump reaches a value of 1.1 for T1Mj09 and a value of 1.4 for T2Mj09. They are visible upstream of the source only for jets at $M_j = 0.9$, which are the jets for which the wavelengths propagating upstream of the source are smallest, being $\lambda_{up}/r_0 \simeq 0.025$. That suggests that these humps are due to a short wavelength compared to the size of the turbulent structures.

The rms values of the scattered pressure normalized by the levels obtained with the mean flow at $M_{90°}$, obtained for $H_e = 2.7$, 8.1 and 24.3 are shown in Fig. 9 as a function of $\psi$. For $H_e = 2.7$ in Fig. 9a, the levels are lower than 0.6 for all angles and jets. The levels for IsoM03 are even lower than 0.07. For $30° \leq \psi \leq 70°$, they increase with the Mach number and the temperature, up to a value of 0.15 for T2Ma09. For $\psi > 100°$, a small hump is visible for all jets except for IsoM03. The peak values of the humps strengthen with the Mach number, reaching 0.58 for IsoM09. They decrease down to 0.23 for T2Ma09. For $H_e = 8.1$, in Fig. 9b, similar trends are observed. However, the levels are higher than in Fig. 9a. Between $\psi = 40°$ and 130°, they increase with the jet Mach number and temperature. As in Fig. 9a, a hump of high 1.3 appears at $\psi > 100°$ for IsoM09. In general, the results obtained for $H_e = 24.3$ in Fig. 9c follow the same trend than those in Figs. 9a and 9b as the Mach number and the temperature vary. However, the levels are higher than 0.5 except for $\psi \leq 15°$. The levels for T1Ma09 and T2Ma09 reach 1.27 near $\psi = 100°$. The levels for IsoM09 have a hump around $\psi = 120°$, as for the other two Helmholtz numbers.

Figure 4 showed that the wavelength upstream of the source is minimal for $M_a = 0.9$, i.e. the isothermal jet at $M_j = 0.9$. When $M_j$ is equal to 0.9, the wavelengths upstream are of the same order of magnitude regardless $T_j$ because $\lambda_{up}$ at most duplicates its length when $T_j$ varies from $T_a$ to $2.25T_a$. Then, the existence of humps only for the jets at Mach number $M_j = 0.9$ in Fig. 8 seems to indicate that they appear when the wavelength-to-radius ratio $\lambda_{up}/r_0$

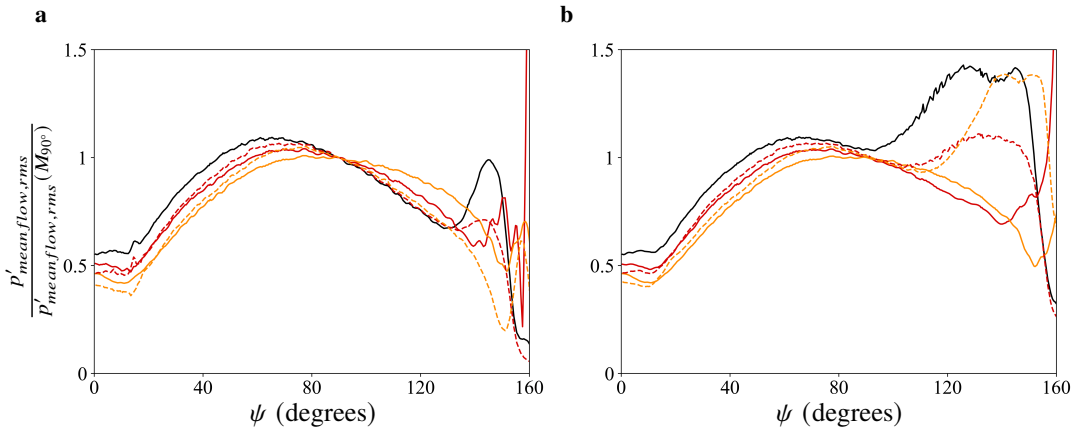


**Fig. 8 Normalized rms pressure levels obtained at $3r_0$ from the source using (a) the mean flow and (b) the flow fluctuations $n_\theta = 0$ for — IsoM09, — T1Ma09, — T2Ma09, - - - T1Mj09 and - - - T2Mj09. The source radiates at $H_e = 8.1$.**

upstream of the source is small. In particular, a hump is visible for IsoM09 when $H_e = 2.7$, where $\lambda_{up}/r_0 = 0.074$. The ratio $\lambda_{up}/r_0$ is lower than 0.074 also for IsoM06 at $H_e = 24.3$, and for IsoM03 at $H_e = 24.3$, as shown in Fig. 4b, but for these cases no hump is visible. This implies that a small wavelength-to-radius ratio is not sufficient to induce the emergence of a hump.

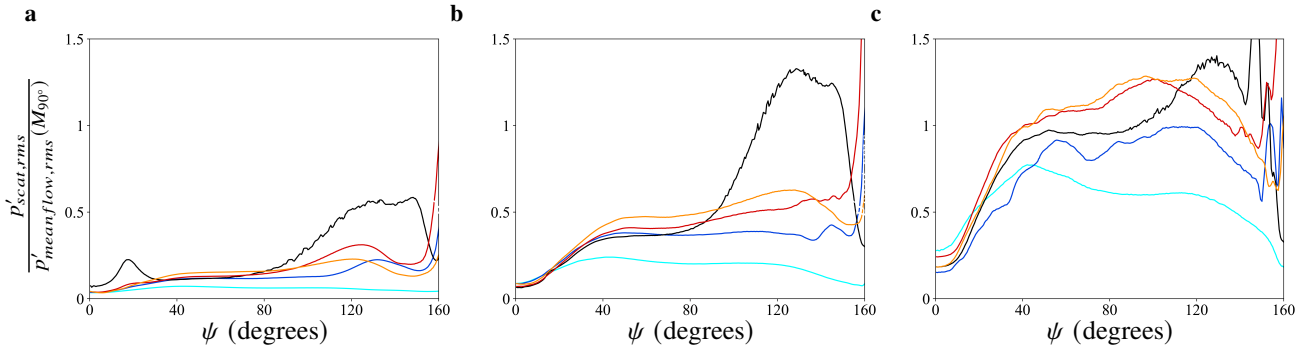


**Fig. 9 Normalized rms pressure levels of the scattered fields for (a) $H_e = 2.7$, (b) $H_e = 8.1$ and (c) $H_e = 24.3$ for the jets — IsoM03, — IsoM06, — IsoM09, — T1Ma09 and — T2Ma09.**

## V. Spectral broadening

### A. Dependence of the observation angle and source frequency

The spectra of the pressure fluctuations $p'_{n_\theta=0}$, normalized by the amplitude of the spectrum of $p'_{meanflow}$ at the source frequency, obtained for IsoM03, IsoM06 and IsoM09 at points $M_{45^\circ}$, $M_{90^\circ}$ and $M_{135^\circ}$ for $H_e = 2.7$ are presented in Fig. 10 as a function of $St_D - St_{D,0}$. In most cases, the spectrum consists of a central tone at the source frequency $St_D = St_{D,0}$ and two broadband lobes on both sides of the tone at $St_D = St_{D,0} \pm \Delta St_D$.

For IsoM03, the lobes moves away from the central tone as the angle $\psi$ increases in Fig. 10a. The distance $\Delta St_D$ varies between 0.45 for $M_{45^\circ}$ and 0.55 at $M_{135^\circ}$. For $\psi = 135^\circ$, the lateral lobe is stronger for $St_D < St_{D,0}$ than for $St_D > St_{D,0}$. The left hand-side lobe reaches $-46dB$, whereas the right hand-side one is $4dB$ lower. At $M_{90^\circ}$, the two lateral maxima reach $-45dB$. Downstream, for $\psi = 45^\circ$, the peak values of the two lobes are also similar and are equal to $-42dB$. These results are consistent with those obtained by Sijtsma [4] and Kroeber [5], where the levels of the lateral lobes were not symmetric at upstream positions for isothermal jets at low Mach number. Downstream they were

symmetric. The position of the maxima of the lateral lobes approaches the central tone as the angle $\psi$ decreases. This was expected because the value $\Delta St_D$ is proportional to the Strouhal number associated with the turbulent structure passing frequency [1]. The turbulent structures size is smaller near the nozzle exit, and thus the passing frequency is higher. In addition, the values of the Strouhal number associated with the turbulent structure passing frequency presented in Fig. 3 are of the same order of magnitude as the values of $\Delta St_D$.

For IsoM06 jet in Fig. 10b, the spectra obtained at $M_{45^\circ}$ and $M_{90^\circ}$ are very similar. The difference in $St_D$ between the lobes and the central tone is $\Delta St_D = 0.6$, and the height of the lobes is of $-37dB$. The spectrum for $M_{135^\circ}$ is superposed with the two previous ones at $St_D < St_{D,0}$, but has a lobe at $St_D > St_{D,0}$ $10dB$ higher that those for $M_{45^\circ}$ and $M_{90^\circ}$. Here, the variation of $\Delta St_D$ with $\psi$ is less important than for IsoM03. This is because at higher Mach numbers, the acoustic waves are convected further downstream before passing through the shear layer than for weak flow velocities. The properties of the turbulence vary more gradually in the space domain downstream of the source, leading to an acoustic field with homogeneous properties throughout the domain.

For IsoM09, in Fig. 10c, the levels in the spectrum increase with $\psi$. For $M_{45^\circ}$, lateral lobes are visible of height $-46dB$. The spectrum for $M_{90^\circ}$ is close to the one for $M_{45^\circ}$ around $St_D = St_{D,0} \pm 0.5$. Away from these two Strouhal numbers, the levels are stronger and the lobes are less marked. For $M_{135^\circ}$, the levels are stronger by at least $10dB$ at $St_D \neq St_{D,0}$ than for $M_{90^\circ}$, and no lobes are visible. When there is a great amount of energy transferred from $St_{D,0}$ to the rest of the frequencies, the scattering is denoted as "strong scattering" [24]. Otherwise, it is denoted as "weak scattering". The spectrum at $M_{90^\circ}$ is between weak and strong scatterings.

To study the effects of the source frequency on haystacking, the spectra obtained for the three isothermal jets at the same positions as in Fig. 10 for $H_e = 8.1$ are plotted in Fig. 11. For IsoM03, in Fig. 11a, the lobes at $St_D > St_{D,0}$ are lower than those one at $St_D < St_{D,0}$. The difference in level is weaker as the angle $\psi$ decreases, similar to that seen in Fig. 10a for $H_e = 2.7$. However, the levels are approximately $10dB$ higher for $H_e = 8.1$. For IsoM06, in Fig. 11b, the three spectra are superposed and have levels $5dB$ higher than for the spectra at $M_{45^\circ}$ and $M_{90^\circ}$ for $H_e = 2.7$. For IsoM09, in Fig. 11c, the lobes at $M_{45^\circ}$ and $M_{90^\circ}$ are centered at the same Strouhal number as those for $M_{45^\circ}$ in Fig. 10c, but here the levels reach $-34dB$. The levels for $St_D \neq St_{D,0}$ for $M_{135^\circ}$ are close to $-30dB$ and lobes are not visible due to the strong scattering.

Finally, the spectra obtained for $H_e = 24.3$ for IsoM03, IsoM06 and IsoM09 are plotted in Figs. 12a, 12b and 12c respectively. The levels are much higher at this source frequency than in the precedent cases. They are higher than $-30dB$ for almost all the Strouhal numbers. For IsoM03, lateral lobes are only visible. As in Figs. 10a and 11a for $H_e = 2.7$ and $H_e = 8.1$, the lobes are also slightly weaker and are further from the central tone as the angle $\psi$ increases. For the other two jets, the spectra at the three positions have levels around $-20dB$. There is a significant decrease in the central peak magnitude compared with the cases at source frequencies $H_e = 2.7$ and 8.1. For IsoM03, the spectrum with the lowest central peak at $-4dB$ also presents the highest lateral lobes. The central tone amplitudes for IsoM06 and for IsoM09 at $M_{45^\circ}$ and $M_{90^\circ}$ are around $-5dB$. For IsoM09 at $M_{135^\circ}$, the central peak is $-11.5dB$ high. Figure 6 shows that the intensity of the scattered field compared with the amplitude of $p'_{meanflow}$ increases with the frequency.

### B. Temperature effects

The effects of the jet temperature on haystacking are now studied. The spectra obtained for the jets IsoM09, T1Ma09 and T2Ma09 at $M_a = 0.9$ for $H_e = 8.1$ are plotted in Fig. 13 as a function of $St_D - St_{D,0}$. The spectra are all characterized by a tone at the source frequency and two lateral lobes. The levels are normalized by the central tone amplitudes $A_{mf}$ obtained for the mean base flow. At $M_{45^\circ}$ and $M_{90^\circ}$, the tone level decrease with respect to $A_{mf}$ is weak for the three jets. At $M_{135^\circ}$, the central tone levels are $1.5dB$ lower than at the two previous positions. The spectra at $M_{45^\circ}$ and $M_{90^\circ}$, in Figs. 13a and 13b, are very similar. Two lobes are observed for all jets and they are almost symmetric relative to the tone. The peak levels of the lobes increase from $-36dB$ for IsoM09 up to $-30dB$ for T2Ma09. This agrees with the trends observed in Fig. 2, where the turbulence intensities increase with the temperature of the jet. At the same time, the difference in Strouhal number between the lobes and the tone $\Delta St_D$ decreases from 0.64 to 0.38. This agrees with the reduction of the Strouhal number associated with the turbulent structure passing frequency in Fig. 3 with rising temperature, because both quantities are proportional. At $M_{135^\circ}$ in Fig. 13c, the lateral lobes for T1Ma09 and T2Ma09 for $St_D < St_{D,0}$ peak at the same frequency as those in Figs.13a and 13b for all jets. However, their levels are $3dB$ higher. In contrast, no lobe is found for IsoM09 on the left-hand side of the tone. For $St_D > St_{D,0}$, the lateral lobes for the three jets are located at the same Strouhal number and have similar levels.

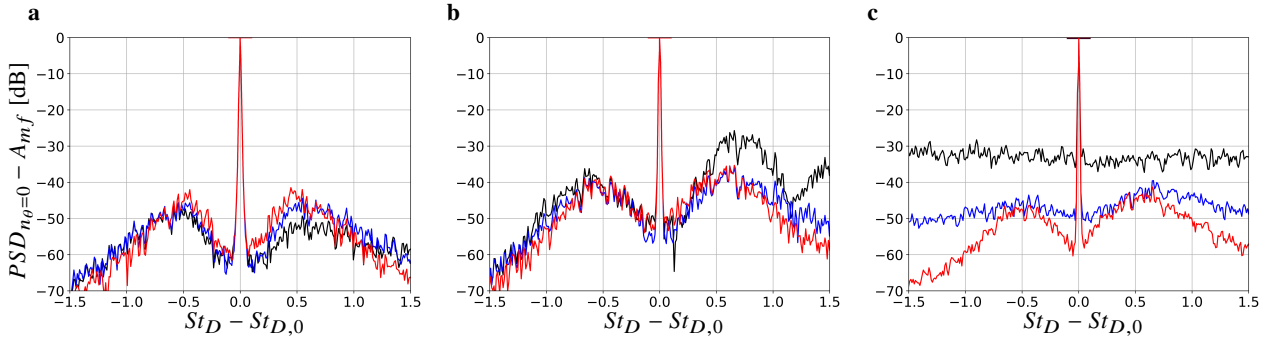


**Fig. 10 Power Spectral Densities obtained at $H_e$ = 2.7 for the jets (a) IsoM03, (b) IsoM06 and (c) IsoM09 at the positions — $M_{45°}$, — $M_{90°}$ and — $M_{135°}$.**

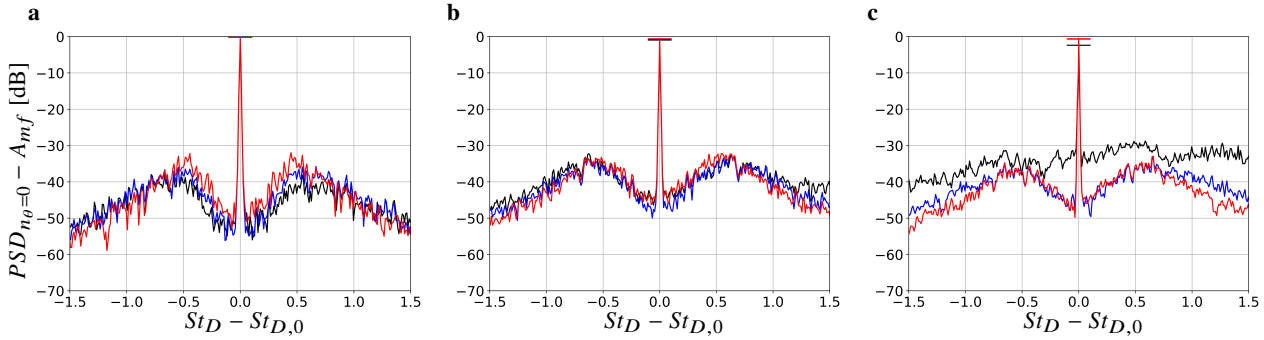


**Fig. 11 Power Spectral Densities obtained at $H_e$ = 8.1 for the jets (a) IsoM03, (b) IsoM06 and (c) IsoM09 at the positions — $M_{45°}$, — $M_{90°}$ and — $M_{135°}$.**

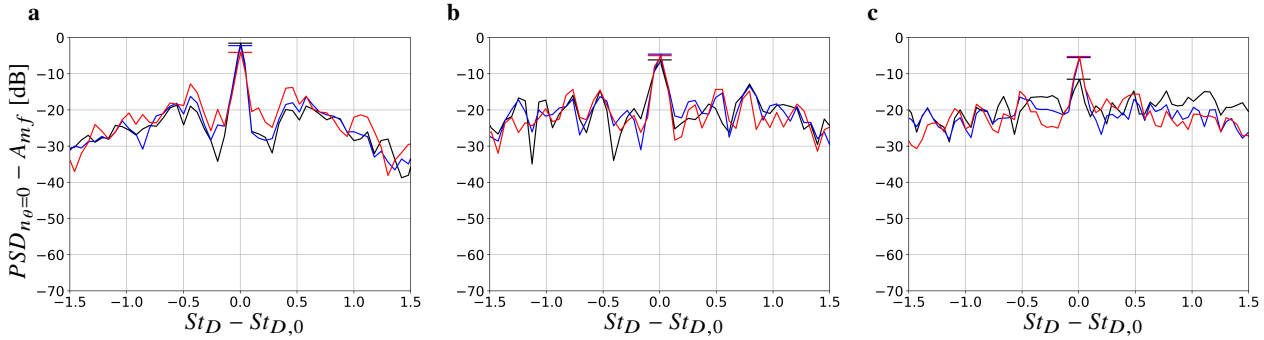


**Fig. 12 Power Spectral Densities obtained at $H_e$ = 24.3 for the jets (a) IsoM03, (b) IsoM06 and (c) IsoM09 at the positions — $M_{45°}$, — $M_{90°}$ and — $M_{135°}$.**

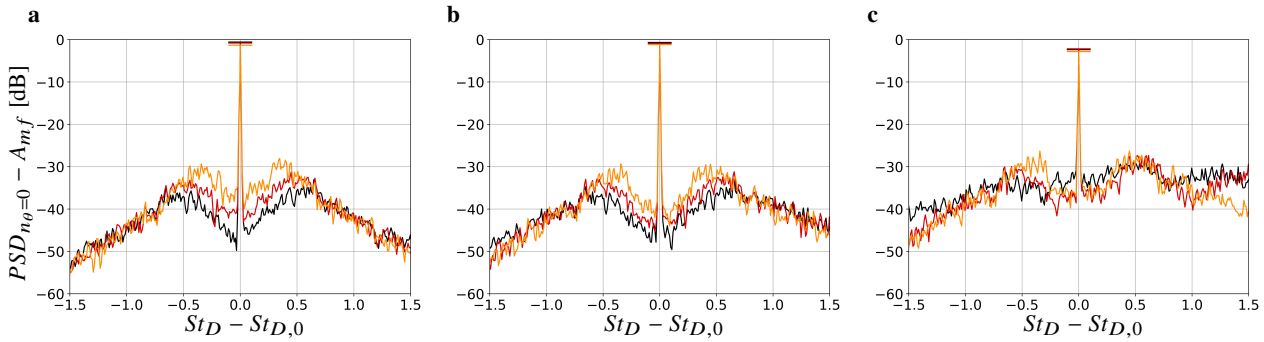


**Fig. 13 Power Spectral Densities obtained at (a) $M_{45°}$, (b) $M_{90°}$ and (c) $M_{135°}$ for the jets — IsoM09, — T1Ma09, — T2Ma09 for $H_e$ = 8.1.**

## VI. Conclusions

This article aims to study the sound scattering by turbulent round jet shear layers for jets at acoustic Mach number $M_a$ varying between 0.3 and 1.3, and temperatures $T_j$ increasing up to 2.25 times the ambient temperature $T_a$. An acoustic source is placed in the jet axis at frequencies yielding Helmholtz numbers $H_e$ = 2.7, 8.1 and 24.3. The spectral densities of the radial velocity and density fluctuations in the jet shear layer are first presented. The pressure fields obtained with and without axisymmetric flow fluctuations in the base flow allow to observe the effects of the turbulence during the spatial scattering. The differences between the two pressure fields appear as beams in the scattered field, and their properties depend on the acoustic Mach number and the source frequency. The directivity of the pressure field is similar when using the mean flow and the axisymmetric mode as base flow, except upstream of the source for jets at Mach number $M_j$ = 0.9. This similarity is not due to a weak spatial scattering because the levels of the scattered field directivity are non-negligible compared to those obtained with the mean flow. The second part of the article focuses on the spectral broadening. The spectra show a tone at the source frequency and two lateral lobes. They are almost symmetric relative to the tone at acoustic Mach numbers $M_a$ greater or equal to 0.6. At $M_a$ = 0.3, this symmetry only happens downstream of the source position. The height of the lobes for isothermal jets varies depending on the source frequency. They also vary with the acoustic Mach number, but their effect is more marked upstream of the source. For jets at $M_a$ = 0.9, the changes observed in the lateral lobes as the temperature increases are related to changes in the turbulence properties.

## Acknowledgment

This work is funded by Siemens Digital Industries Software through the Ph.D. program CIFRE 2021/0106. It was granted access to the HPC resources of PMCS2I (Pôle de Modélisation et de Calcul en Sciences de l'Ingénieur de l'Information) of École Centrale de Lyon. The authors would like to acknowledge S. Le Bras for her close and careful supervision of this work. For the purpose of Open Access, a CC-BY public copyright license has been applied by the authors to the present document and will be applied to all subsequent versions up to the author-accepted manuscript arising from this submission.

## References

[1] Candel, S., Julienne, A., and Guedel, A., "Refraction and scattering of sound in an open wind tunnel flow," *ICIASF 1975; 6th International Congress on Instrumentation in Aerospace Simulation Facilities*, 1975, pp. 288–300.

[2] Candel, S., Guedel, A., and Julienne, A., "Radiation, refraction and scattering of acoustic waves in a free shear flow," *3rd AIAA aeroacoustics Conference*, AIAA 76-544, Palo Alto,CA,U.S.A., 1976. https://doi.org/10.2514/6.1976-544.

[3] Candel, S., Guedel, A., and Julienne, A., "Résultats préliminaires sur la diffusion d'une onde acoustique par écoulement turbulent," *Le Journal de Physique Colloques*, Vol. 37, No. C1, 1976, pp. 153–160. https://doi.org/10.1051/jphyscol:1976122.

[4] Sijtsma, P., Oerlemans, S., Tibbe, T. G., Berkefeld, T., and Spehr, C., "Spectral broadening by shear layers of open jet wind tunnels," *20th AIAA/CEAS aeroacoustics Conference*, AIAA 2014-3178, Atlanta, GA, U.S.A., 2014. https://doi.org/10.2514/6.2014-3178.

[5] Kroeber, S., Hellmold, M., and Koop, L., "Experimental investigation of spectral broadening of sound waves by wind tunnel shear layers," *19th AIAA/CEAS Aeroacoustics Conference*, AIAA 2013-2255, Berlin, Germany, 2013. https://doi.org/10.2514/6.2013-2255.

[6] Bennaceur, I., Mincu, D. C., Mary, I., Terracol, M., Larchevêque, L., and Dupont, P., "Numerical simulation of acoustic scattering by a plane turbulent shear layer: spectral broadening study," *Computers & Fluids*, Vol. 138, 2016, pp. 83–98. https://doi.org/10.1016/j.compfluid.2016.08.012.

[7] Clair, V., and Gabard, G., "Computational study of the spectral broadening of an acoustic tone by turbulence," *Proceedings of the ICSV22*, Florence, Italy, 2015, p. 8.

[8] Ewert, R., Kornow, O., Tester, B. J., Powles, C. J., Delfs, J., and Rose, M., "Spectral broadening of jet engine turbine tones," *14th AIAA/CEAS aeroacoustics Conference*, AIAA 2008-2940, Vancouver, Canada, 2008. https://doi.org/10.2514/6.2008-2940.

[9] Bogey, C., Marsden, O., and Bailly, C., "Large-eddy simulation of the flow and acoustic fields of a Reynolds number 105 subsonic jet with tripped exit boundary layers," *Physics of Fluids*, Vol. 23, No. 3, 2011, p. 035104. https://doi.org/10.1063/1.3555634.

[10] Bogey, C., and Marsden, O., "Numerical investigation of temperature effects on properties of subsonic turbulent jets," *19th AIAA/CEAS Aeroacoustics Conference*, AIAA 2013-2140, Berlin, Germany, 2013. https://doi.org/10.2514/6.2013-2140.

[11] Bogey, C., "Grid sensitivity of flow field and noise of high-Reynolds-number jets computed by large-eddy simulation," *International Journal of Aeroacoustics*, Vol. 17, No. 4, 2018, pp. 399–424. https://doi.org/10.1177/1475472X18778287.

[12] Bogey, C., "Tones in the acoustic far field of jets in the upstream direction," *AIAA Journal*, Vol. 60, No. 4, 2022, pp. 2397–2406. https://doi.org/10.2514/1.J061013.

[13] Bogey, C., "Acoustic tones in the near-nozzle region of jets: characteristics and variations between Mach numbers 0.5 and 2," *Journal of Fluid Mechanics*, Vol. 921, 2021, p. A3. https://doi.org/10.1017/jfm.2021.426.

[14] Bogey, C., "Interactions between upstream-propagating guided jet waves and shear-layer instability waves near the nozzle of subsonic and nearly ideally expanded supersonic free jets with laminar boundary layers," *Journal of Fluid Mechanics*, Vol. 949, 2022, p. A41. https://doi.org/10.1017/jfm.2022.776.

[15] Bogey, C., "A study of the effects of temperature on velocity and density fluctuations in high-subsonic jets," *52nd Aerospace Sciences Meeting*, AIAA 2014-0524, National Harbor, Maryland, U.S.A., 2014, p. 0524. https://doi.org/10.2514/6.2014-0524.

[16] Bogey, C., "Properties of the tones emerging in the near-field pressure spectra of hot high-speed jets," *Tech. rep., AIAA Paper*, 2024.

[17] Camussi, R., and Bogey, C., "Intermittent statistics of the 0-mode pressure fluctuations in the near field of Mach 0.9 circular jets at low and high Reynolds numbers," *Theoretical and Computational Fluid Dynamics*, Vol. 35, No. 2, 2021, pp. 229–247. https://doi.org/10.1007/s00162-020-00553-9.

[18] Panda, J., and Seasholtz, R. G., "Experimental investigation of density fluctuations in high-speed jets and correlation with generated noise," *Journal of Fluid Mechanics*, Vol. 450, 2002, pp. 97–130. https://doi.org/10.1017/S002211200100622X.

[19] Williamschen, M., "Time-domain DGM for turbofan exhaust noise predictions," Phd, University of Southampton, Aug. 2018.

[20] Goldstein, M. E., *aeroacoustics*, McGraw-Hill, New York, 1976.

[21] Bogey, C., and Bailly, C., "A family of low dispersive and low dissipative explicit schemes for flow and noise computations," *Journal of Computational Physics*, Vol. 194, No. 1, 2004, pp. 194–214. https://doi.org/10.1016/j.jcp.2003.09.003.

[22] Hesthaven, J. S., and Warburton, T., *Nodal discontinuous Galerkin methods: Algorithms, analysis, and applications*, Texts in applied Mathematics, Springer-Verlag, New York, 2008. https://doi.org/10.1007/978-0-387-72067-8.

[23] Martin-Martin, L., Clair, V., Bogey, C., and Gabard, G., "Numerical study of the scattering of acoustic waves by an elliptic vortex." *The Journal of the Acoustical Society of America*, Vol. 155, No. 3, 2024, pp. 1707–1718. https://doi.org/https://doi.org/10.1121/10.0025138.

[24] McAlpine, A., Powles, C. J., and Tester, B. J., "A weak-scattering model for turbine-tone haystacking," *Journal of Sound and Vibration*, Vol. 332, No. 16, 2013, pp. 3806–3831. https://doi.org/10.1016/j.jsv.2013.02.023.